NIH Public Access
Author Manuscript
J Micromech Microeng. Author manuscript; available in PMC 2012 November 23.

Published in final edited form as:
J Micromech Microeng. 2011 June 1; 21(6): . doi:10.1088/0960-1317/21/6/067004.

Amplifying transmission and compact suspension for a low-profile, large-displacement piezoelectric actuator

J F Domke[1], **C-H Rhee**[2], **Z Liu**[3], **T D Wang**[3], and **K R Oldham**[2]

J F Domke: domkej@umich.edu; K R Oldham: oldham@umich.edu

[1]Department of Microsystems Engineering, University of Freiburg - IMTEK, Georges-Koehler-Allee 102, 79110 Freiburg, Germany, visiting scholar at the Department of Mechanical Engineering, University of Michigan, 2350 Hayward Ave, Ann Arbor, MI 48109, USA

[2]Department of Mechanical Engineering, University of Michigan, 2350 Hayward Ave, Ann Arbor, MI 48109, USA

[3]Department of Biomedical Engineering, University of Michigan, Ann Arbor, MI 48109, USA

Abstract

A low-profile, piezoelectrically-driven microactuator is presented that achieves very large stroke lengths within size constraints suitable for certain endoscopic microscopy applications. The actuator utilizes a transmission consisting of lever arm and chevron-beam structures to amplify high-force, low-displacement motion of a ceramic lead-zirconate-titanate (PZT) brick into large displacement of a translational platform. For ±120 V input, a full range of 486 μm of motion is achieved, with natural frequency greater than 500 Hz. This corresponds to an anticipated In addition, the lateral translational platform is supported by a redesign of common folded silicon flexures to provide large transverse and vertical stiffness when the width of the actuator is limited.

1. Introduction

A silicon transmission coupled with a piezoelectric ceramic is designed and tested for large displacement actuation within endoscopic microscopy space requirements. Several types of novel imaging modalities enable deep optical penetration (up to 500 μm) into biological tissue [1], including dual-axes confocal microscopy and two-photon microscopy [2, 3, 4, 5]. Large, high-speed displacement of optical components such as mirrors or lenses via microactuation could rapidly change such microscopes' depth-of-focus to produce real-time cross-sectional or three-dimensional images.

One proposed endoscopic instrument is a two-photon microscope with its optical path occupying the center of the imaging system; actuators that fit along the side of the optical path minimize total cross-sectional area and volume of the scanning head used to generate images. Such actuators would need a cross-sectional area of approximately 3 mm by 0.6 mm or smaller, and a length less than 20 mm, to avoid increasing scanning head size when implementing into-tissue scanning. Scanning range should be nearly 500 μm, at an unloaded frequency of at least 100 Hz. This corresponds to real-time scanning of 10 Hz or better when equipped with a 3 mm diameter, 0.12g focusing lens, and a projected optical scanning distance in tissue of 220 μm.

The combination of stroke length and speed desired exceeds that demonstrated by previous miniature actuators of the size desired. For example, large displacement thermal actuator speed is limited by the thermal time constant of the devices and heat generated may be difficult to dissipate *in vivo* [9, 13]. Piezoelectric stack actuators and DC-linear motors used in previous miniaturized optical imaging systems do not meet the space requirements and

$watermark-text
$watermark-text
$watermark-text

$watermark-text

$watermark-text

$watermark-text

would increase probe volume [6, 7]. Electrostatic actuator mechanisms are well established for a wide range of stroke lengths [15, 8], but suffer from limited force side-instability at very large displacements.

The actuator described here relies on the large work density of piezoelectric materials, and converts small-displacement, large-force motion of a lead-zirconate-titanate (PZT) ceramic into large displacement motion via a micro-machined silicon transmission. The actutator optimizes a combination of lever-arm and bridge-type amplification mechanisms. Both types of amplification have been previously used in micro-scale systems, such as [16, 17, 18], and the optimized mechanism combining their effects shows amplification ratios exceeding those previously described for fabricated MEMS devices. In addition, a folded flexure design is adapted from conventional arrangements to fit in the long but comparatively narrow space available for the two-photon microscopy application. To illustrate the benefits of this approach, Table 1 compares the cross-section, displacement, natural frequency, and amplification ratios of existing large stroke or large amplification microactuators.

2. Transmission Design

The ability to perform endoscopic tissue imaging using a fiber-coupled two-photon laser has recently been demonstrated by several research groups as [19, 20, 21]. For many applications the size of the scanning mechanism for image creation is a limiting factor in system miniaturization. Many projects concentrate on automated x- and y- scanning, but a fast enough scanning mechanism parallel to the optical path could ultimately lead to 3-dimensional imaging of tissue structures *in vivo*, with novel diagnostic capabilities for allergic diseases and cancer. Figure 1 shows the schematic drawing of a scanning probe suggested by the Biomedical Research Team at the University of Michigan; a MEMS mirror unit performs x- and y- direction scanning, while a large displacement linear actuator drives a lens to adjust the focal depth during scanning.

We suggest a linear actuator design consisting of three parts: a piezoelectric material to generate a motion, an amplification structure that uses lever-arm and chevron bridge-structures to transform the motion and a platforms that allows the fixation and stabilization of a micro-lens. Figure 2a) and b) illustrate the first amplification stage. Two short, parallel flexures are placed a small distance apart, one connecting a lever-beam to a fixed base and the other connecting the lever-beam to a nose that is actuated by a piezo (piezo not shown in this illustration). Using the lever-effect the lateral displacement of the piezo is transformed into a large transverse displacement of the two lever-tips. As shown in c), the transverse movement of the lever-tips is then re-transformed into a lateral movement of the amplifier-tip using a second, chevron bridge-type amplification structure.

For analytical modeling for device optimization a linear mathematical expression was found relating the input of the amplifier to its output taking forces, moments and displacements into consideration (figure 3).

The in-plane deflection and rotation of the *i*'th flexural element in the design was defined in terms of a stiffness matrix, K_i, using linear beam relationships,

$$K_i^{-1} = \begin{bmatrix} \frac{L_i^3}{3EI_i} & 0 & -\frac{L_i^2}{2EI_i} \\ 0 & \frac{L_i}{EA_i} & 0 \\ -\frac{L_i^2}{2EI_i} & 0 & \frac{L_i}{EI_i} \end{bmatrix} \quad (1)$$

$watermark-text

$watermark-text

$watermark-text

where L_i, A_i and I_i are the ith flexure's length area and area moment of inertia of the ith flexure and E is silicon's elastic modulus. Forces and displacements at the flexural elements, $F_i=[\ F_{x,i}\quad F_{y,i}\quad M_i\ ]^T$ and $X_i=[\ x_i\quad y_i\quad \theta_i\ ]^T$, respectively, are then

$$\begin{aligned} F_1&=K_1(X_1-X_0)\\ F_2&=K_2X_2\\ R_1^{-1}F_4&=K_3\,(R_1^{-1}X_4-R_1^{-1}X_3)\\ R_2^{-1}F_6&=K_4\,(R_2^{-1}X_6-R_2^{-1}X_5) \end{aligned} \quad (2)$$

where R_1 and R_2 are rotation matrices. Geometric relationships for small angular rotations are enforced by a second set of matrix equations,

$$\begin{aligned} X_2&=S_{2,1}X_1\\ X_3&=S_{3,1}X_1\\ R_1^{-1}X_5&=S_{5,4}R_1^{-1}X_4 \end{aligned} \quad (3)$$

where $S_{i,j}$ relates the displacement of two points on the same rigid body to their x- and y-offsets, $L_{x(i,j)}$ and $L_{y(i,j)}$,

$$S_{i,j}=\begin{bmatrix} 1 & 0 & L_{y(i,j)}\\ 0 & 1 & L_{x(i,j)}\\ 0 & 0 & 1 \end{bmatrix}. \quad (4)$$

Finally, force balances about each rigid body are completed and written

$$\begin{aligned} -F_0+T_1F_1&=0\\ -F_1+T_2F_2+T_3F_3&=0\\ -R_1^{-1}F_3+T_4R_1^{-1}F_4&=0\\ -R_1^{-1}F_4+T_5R_1^{-1}F_5&=0\\ -R_2^{-1}F_5+T_6R_2^{-1}F_6&=0 \end{aligned} \quad (5)$$

where T matrices include small displacement moment arm lengths to perform moment balance calculations.

The system of linear equations provided by (2), (3) and (5) may be solved to relate piezoelectric ceramic force and displacement, F_0 and X_0, to platform displacement, X_6 against a load force, F_6.

In particular, x-displacement of the platform, x_6, is obtained when transverse and rotational motion of platform and piezoelectric ceramic (y_6, θ_6, y_0 and θ_0) are constrained to zero by symmetry. In addition, the relationship between the piezoelectric displacement, x_0 and the opposing lateral force on the piezoelectric actuator, F_0, are related using piezoelectric strain coefficient, $d_{3,1}$, to be

$$x_0=d_{3,1}\frac{V}{t_{PZT}}L_{PZT}+F_0\frac{L_{PZT}}{E_{PZT}A_{PZT}} \quad (6)$$

where V is applied voltage, t_{PZT}, L_{PZT}, A_{PZT} and E_{PZT} are thickness, length, cross-sectional area, and elastic modulus of the PZT ceramic.

$watermark-text

$watermark-text

$watermark-text

The full analytical model agrees with finite element models, save for slight overstatement of platform deflection (~ 10%) due to the neglect of any deformation in the long lever arms. Linear simulations were also compared to nonlinear simulation results, with only small differences, as shown in figure 5. Likewise, stress within the flexural beams was calculated from the intermediate forces in the system equations, again with close agreement to full finite-element simulations, permitting design optimization with maximum stress limits.

3. Platform Suspension Design

In an endoscopic imaging system, two parallel piezoelectric linear actuators drive the focusing lens resting on the moving platform. The typical lens mass approximates 20 mg. Thus, a suspension system with a low spring constant in the actuation (lateral) direction and a high spring stiffness in the vertical and transverse direction is required. Figure 4a) shows one of the most common MEMS suspension designs, supporting a platform at each corner with a folded flexure. This kind of suspension provides a relatively low vertical and transverse spring constant due to the short and meander-shaped spring structures forced by the relatively narrow width of the actuator.

The spring constant k of a set of folded flexures can be given by

$$k = \frac{E\, t\, w^3}{l^3} \frac{N_{legs}}{N_{folds}} \quad (7)$$

where t is the thickness, w the width and l the length of a single fold of the flexure. To increase transverse and vertical stiffness, additional springs may be added to each link in the folded flexure, forming a double spring system. Lateral stiffness may be kept low by capitalizing on the nonlinear dependence of stiffness on length, with the result that for N times as many springs per link, new length L' need only be increased according to

$$l'/l = N^{\frac{1}{3}} \quad (8)$$

to maintain a constant lateral spring constant, all other dimensions being equal. This additional length is accommodated, or even exceeded, by interlacing sets of double springs. Illustrations 4 b) and c) show improved spring layouts for actuators with constrained side-to-side dimensions. The alternate designs use the maximal available length for springs but also providing the platform with a high vertical and transverse spring constant by using a double-spring suspension. Table 2 compares the spring constants and dimensions of the three different suspension systems shown. High transverse and vertical spring constants and high lateral flexibility make design 3 suitable for carrying and guiding a lens that will be fixed perpendicular to the platform's surface.

4. Design Optimization

To optimize the performance of the amplification stage 14 design parameters, including suspension lengths and widths and distances between spring connections to the rigid portion of the transmission were optimized. The optimization used the analytical model, linear simulations and non-linear simulations. Sweeping the values of single parameters in the analytical model identified its sensitivity to each variable. High influence parameters were then analyzed in Design of Experiments software JMP to optimize their values when accounting for mutual influences. A non-linear simulation was used to verify the performance of the final optimized set of parameters (figure 6). Table 3 shows key dimensions of the resulting actuator used for experiments (minimum beam width of 8 μm).

$watermark-text

$watermark-text

$watermark-text

5. Fabrication and Assembly

A Silicon-On-Insulator process is used to fabricate the amplifier and platform structure, with a 100 μm thick device-layer and 3 μm thick SiO_2 buried oxide layer. Wafers are coated with Low-pressure chemical-vapor-deposited silicon oxide, for better protection during deep-reactive ion-etching (DRIE), and gold pads are deposited via a lift-off procedure to provide electrical conduction to the underside of the PZT ceramic. The transmission, suspension, and platform geometry is then patterned into the device-layer by DRIE. The backside of the actuators (handle-wafer) is also patterned by DRIE to remove material behind the PZT connection point and the moving platform, reducing the odds of adhesive impeding moving parts. Hydrofluoric Acid (HF) is then used to etch the SiO_2 by a timed etch, followed by critical point drying. Minimal surviving feature sizes from the device layer DRIE were 6 μm, used for spring design. Due to long etching times a slight lateral overetching of 1–2 μm and some footing were observed during the DRIE process. The actuator on the wafer is surrounded by an etching trench and automatically detaches from the wafer which replaces dicing.

Figure 7 shows a completed actuator consisting of the PZT, the two amplification stages and the lens platform. The PZT strip has dimensions of 150 μm × 3 mm × 10 mm. Its piezoelectric coeffcient d_{31} is $2.1 \cdot 10^{-10}$ C/N and when actuated at 110 V a displacement of 1.5 μm can be obtained against the stiffness of the transmission. The PZT is connected to the handle layer on one end and fixed to a movable platform in the device-layer at the other end pushing or pulling the mechanical amplifier. Silver conductive adhesive is used for the fixation of the piezo.

6. Experimental Results

To characterize the design different tests have been performed using voltages up to 100 V. Figure 8 shows a picture of the top part of the moving actuator. The displacement of the device is determined by a high speed microscope camera using a scale that was fabricated in a gold layer on top of the actuator. The pictured version of the actuator also includes electrostatic feedback structures integrated in the lens platform that allow automated position readout.

A comparison between the measured values for the platform-displacement and the calculated and simulated results is shown in figure 9. Figure 9 is plotted in a voltage range from −100 V to 100 V. The measured DC platform-displacement is indicated by the black squares. At ±100 V the PZT displacement is $\mp$1.43 μm and the platform displacement ±243 μm which equals a total platform displacement of 486 μm and an amplification ratio of 170 (all values are DC values). The measured displacement is very similar to the calculated and simulated ones. The slightly higher displacement of the real system can be explained by the lateral and vertical thinning during fabrication. Although the flexural lever arm, chevron, and suspension springs have nominal widths of 8,8, and 12 μm, overetching and sidewall erosion during the DRIE step leads to a more flexible structure, similar to a design with widths of 6, 6, and 8 μm.

An AC characteristic of the device is shown in figure 10. A supply voltage of 3 V is applied to the electrical contacts of the PZT and the frequency is swept from 1 to 800 Hz. Whereas the displacement for 3 V at 10 Hz is only 7.5 μm a distinct resonance frequency can be found at 507 Hz with an actuator displacement of 370 μm (no lens included). Although in practice the actuator will be operated below resonance, a high resonance frequency is required in order to allow accurate DC-scanning at video frequencies (~10 Hz) when carrying a lens. Experimentally, when a 0.12 g mass is added to a single actuator, natural frequency is measured at greater than 37 Hz, compared to an anticipated 43 Hz.

$watermark-text

$watermark-text

$watermark-text

In addition to the nominal actuator design, with thickness of 0.6 mm, width of 3 mm and length of 23 mm, two alternative, more compact designs were fabricated. One places the lens-platform within the amplifier (middle) and another one with the 150 μm thick piezo situated in the 500 μm thick handle layer (bottom). For this shortest design, a stack of piezo strips could be used without increasing the dimensions of the system (up to 3 piezo strips on top of each other), while remaining within a total length of 12 mm.

7. Conclusion

In this paper we have presented the design and fabrication of a piezoelectric actuator for miniature two-photon microscopy. The actuator consists of a PZT, a mechanical amplification mechanism and a suspended lens-platform. The mechanical amplification has been optimized by an analytical model and linear and nonlinear simulations. The entire actuator has been fabricated using a SOI process and then characterized. With an amplification factor of 170x, the amplifier is able to transform a PZT input displacement of 1.43 μm (at 100 V) into a lens-platform displacement of 486 μm. This nominal design meets the specifications needed for the integration into a two-photon endoscope probe to allow 3-dimensional imaging. Other designs have also been fabricated that reduce actuator volume to as little as 0.6 mm × 3 mm × 12 mm.

References

1. Theer, Patrick; Hasan, Mazahir T.; Denk, Winfried. Two-photon imaging to a depth of 1000 microm in living brains by use of a ti:al2o3 regenerative amplifier. Opt Lett. Jun; 2003 28(12):1022–1024. [PubMed: 12836766]
2. Claxton, Nathan S.; Fellers, Thomas J.; Davidson, Michael W. Laser scanning confocal microscopy. Microscopy. 2006; 1979(21):1–37.
3. Denk W, Strickler JH, Webb WW. Two-photon laser scanning fluorescence microscopy. Science. Apr; 1990 248(4951):73–76. [PubMed: 2321027]
4. Helmchen, Fritjof; Denk, Winfried. Deep tissue two-photon microscopy. Nat Methods. Dec; 2005 2(12):932–940. [PubMed: 16299478]
5. Fu L, Gu M. Fibre-optic nonlinear optical microscopy and endoscopy. J Microsc. Jun; 2007 226(Pt 3):195–206. [PubMed: 17535259]
6. Faulhaber. Linear dc servomotors. 2006. www.faulhaber-group.com
7. Henderson, DA. Novel piezo motor enables positive displacement microfluidic pump. Presented at NSTI Nanotech; 2007; 2007.
8. Smith, Gabe; Maloney, John; Fan, Lawrence; DeVoe, Don L. Large displacement microactuators in deep reactive ion etched single crystal silicon. Proceedings of SPIE. 2001; 4559
9. Hubbard, NB.; Howell, LL. Design and characterization of a dual-stage, thermally actuated nanopositioner.
10. Traina ZJ, Conway NJ, Kim S-G. A strain amplifying piezoelectric mems actuator. J Micromech Microeng. 2007; 17:781–787.
11. Li Z, Rodgers SM, Kota S, Joo J, Sniegowski J. Design of compliant mechanisms: applications to mems. Analog Int Circuits Signal Proc. 2001; 29(1–2):7–15.
12. Ono T, Sabri M, Esashi M. Microassembly of pzt actuators into silicon microstructures. IEEJ Trans Sensors Micromachines. 2009; 129(12):471–472.
13. Hetrick JZ, Chu LL, Gianchandani YB. High amplification compliant microtransmission for rectilinear electrothermal actuators. Sensors Actuators A. 2002; 97–98:776–783.
14. Su X-PS, Yang HS. Design of compliant microleverage mechanisms. Sensors Actuators A. 2001; 87:146–156.
15. Grade, John D.; Jerman, Hal; Kenny, Thomas W. Design of large deflection electrostatic actuators. JOURNAL OF MICROELECTROMECHAN-ICAL SYSTEMS. 2003; 12

$watermark-text

$watermark-text

$watermark-text

16. Maa, Hong-Wen; Yao, Shao-Ming; Wang, Li-Quan; Zhongb, Zhi. Analysis of the displacement amplification ratio of bridge type flexure hinge. Sensors and Actuators. 2006; 132:730–736.

17. Yu, HG.; Mc-Kinstry, S Trolier. IEEE. 2005. Mems flextensional actuator using lead zirconate titanate thin film; p. 375-378.

18. Bolzmacher C, Bauer K, Schmid U, Hafez M, Seidel H. Displacement amplification of piezoelectric microactuators with a micromachined leverage unit. Sensors and Actuators. 2009:61–67.

19. Hoy, Christopher L.; Durr, Nicholas J.; Chen, Pengyuan; Piyawattanametha, Wibool; Ra, Hyejun; Solgaard, Olav; Ben-Yakar, Adela. Miniaturized probe for femtosecond laser microsurgery and two-photon imaging. Opt Express. Jun; 2008 16(13):9996–10005. [PubMed: 18575570]

20. Jung, Woonggyu; Tang, Suo; Mc-Cormic, Daniel T.; Xie, Tiquiang; Ahn, Yeh-Chan; Su, Jianping; Tomov, Ivan V.; Krasieva, Tatiana B.; Tromberg, Bruce J.; Chen, Zhong-ping. Miniaturized probe based on a microelectromechanical system mirror for multiphoton microscopy. Opt Lett. Jun; 2008 33(12):1324–1326. [PubMed: 18552946]

21. Piyawattanametha, Wibool; Cocker, Eric D.; Burns, Laurie D.; Barretto, Robert P.; Jung, Juergen C.; Ra, Hyejun; Solgaard, Olav; Schnitzer, Mark J. In vivo brain imaging using a portable 2.9 g two-photon microscope based on a microelectromechanical systems scanning mirror. Opt Lett. Aug; 2009 34(15):2309–2311. [PubMed: 19649080]

$watermark-text
$watermark-text
$watermark-text

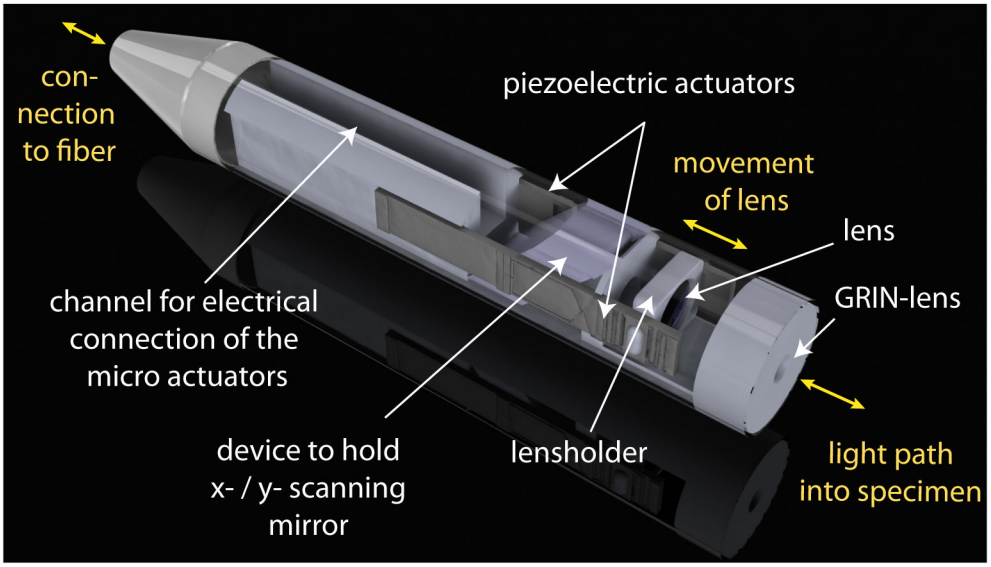

Figure 1.
Schematic drawing of a 3-dimensional scanning two-photon endoscope with an x- and y-scanning mirror and a focusing lens.

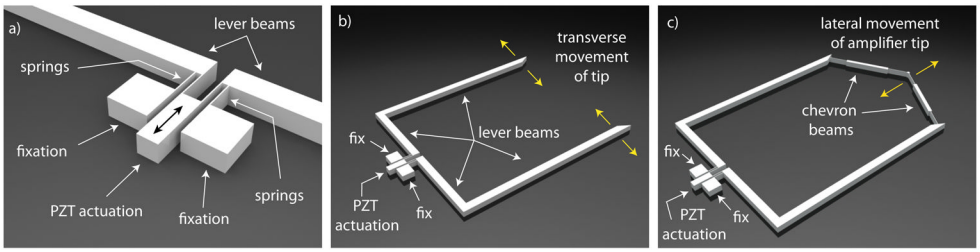

Figure 2.
Transmission design consisting of (a,b) lever and (c) chevron bridge structures to amplify PZT motion.

$watermark-text
$watermark-text
$watermark-text

$watermark-text
$watermark-text
$watermark-text

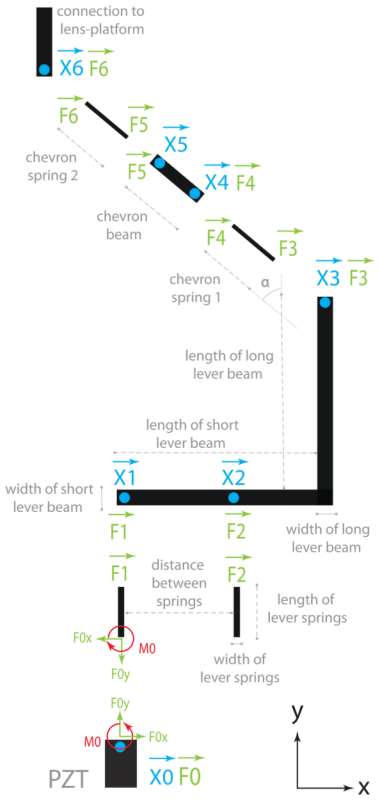

Figure 3.
Amplifier structural model (symmetric)

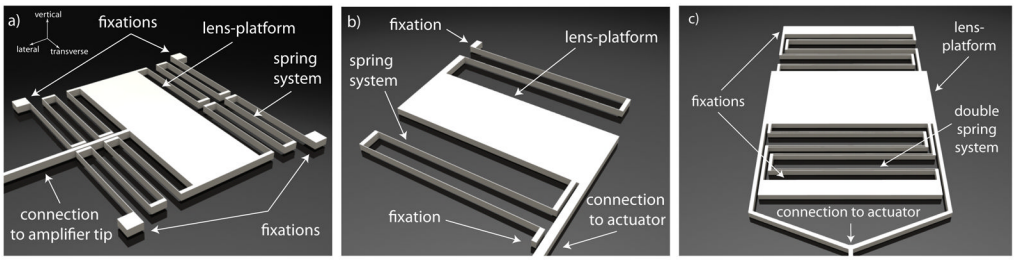

Figure 4.
Candidate suspension designs for the lens platform using various folded-flexure configurations, with (c) showing an optimized suspension consisting of double springs to use the maximal space available while maintaining stiffness in undesired directions.

$watermark-text
$watermark-text
$watermark-text

$watermark-text

$watermark-text

$watermark-text

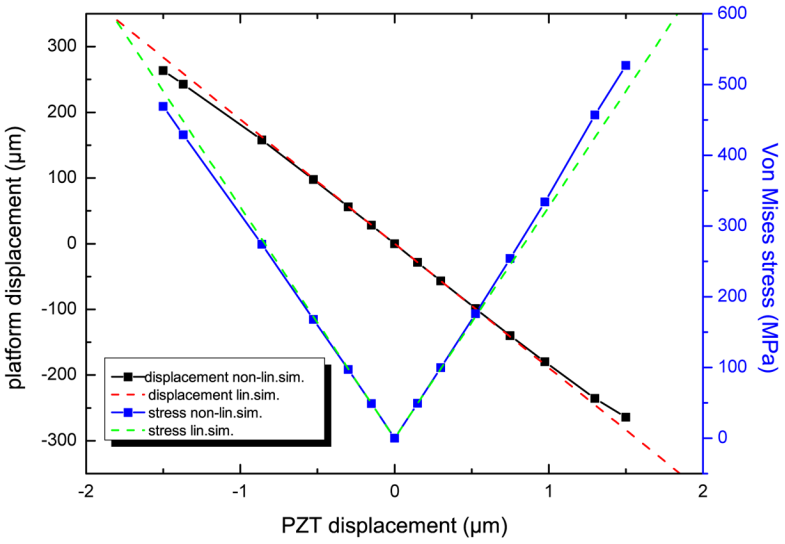

Figure 5.
Comparison of linear and nonlinear finite-element simulation of platform displacement and the maximal Von Mises stress for a sample transmission design.

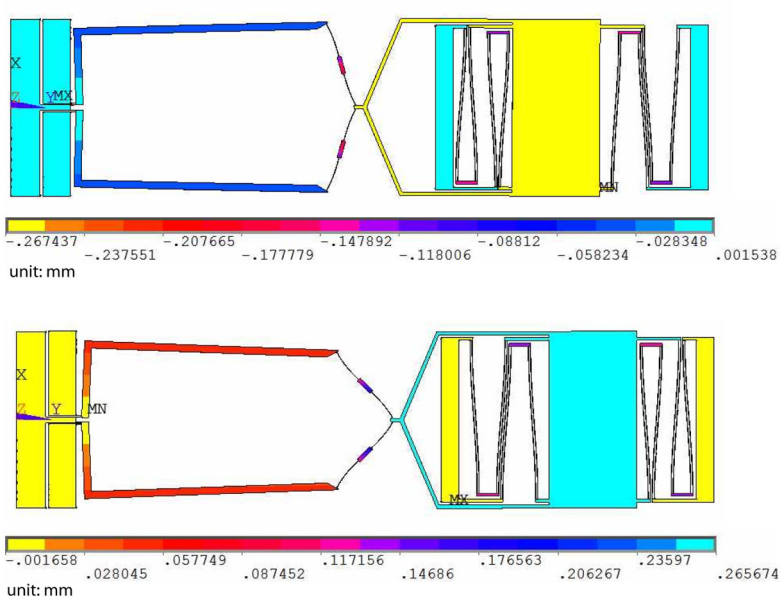

Figure 6.
Non-linear ANSYS simulation of the mechanical amplifier, converting input displacement of 1.5 μm to platform-displacement of about 265 μm. Top: PZT pulls, Bottom: PZT pushes.

$watermark-text
$watermark-text
$watermark-text

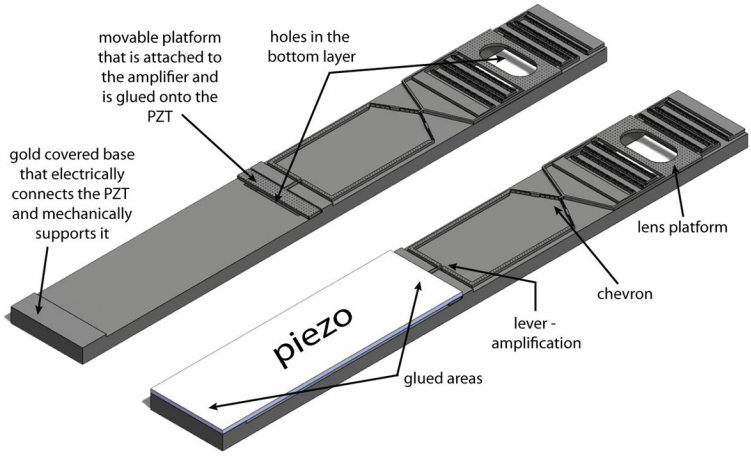

Figure 7.
Entire actuator design consisting of the piezo, the amplifier and the lens-platform.

$watermark-text
$watermark-text
$watermark-text

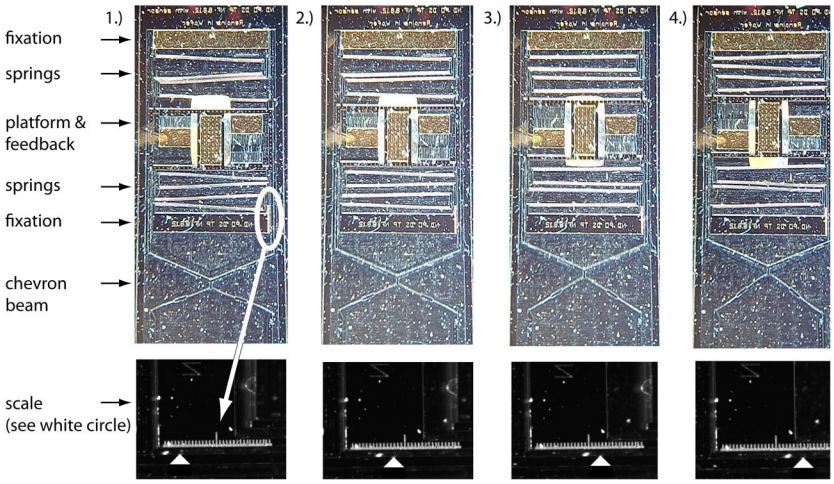

Figure 8.
Piezoelectric actuator motion at 80 V, a scale helps to determine the distance traveled by the platform (small scale bars: 5 μm, large scale bars: 20 μm).

$watermark-text
$watermark-text
$watermark-text

$watermark-text
$watermark-text
$watermark-text

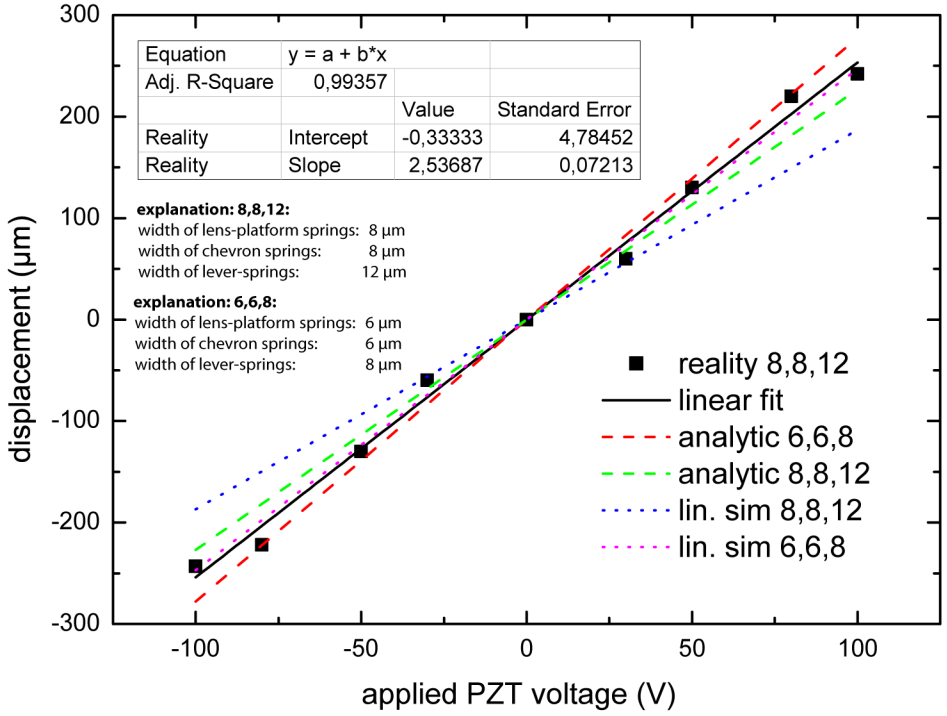

Figure 9.
Comparison of the measured displacement of the actuator with the results of the analytical model and the simulation.

$watermark-text

$watermark-text

$watermark-text

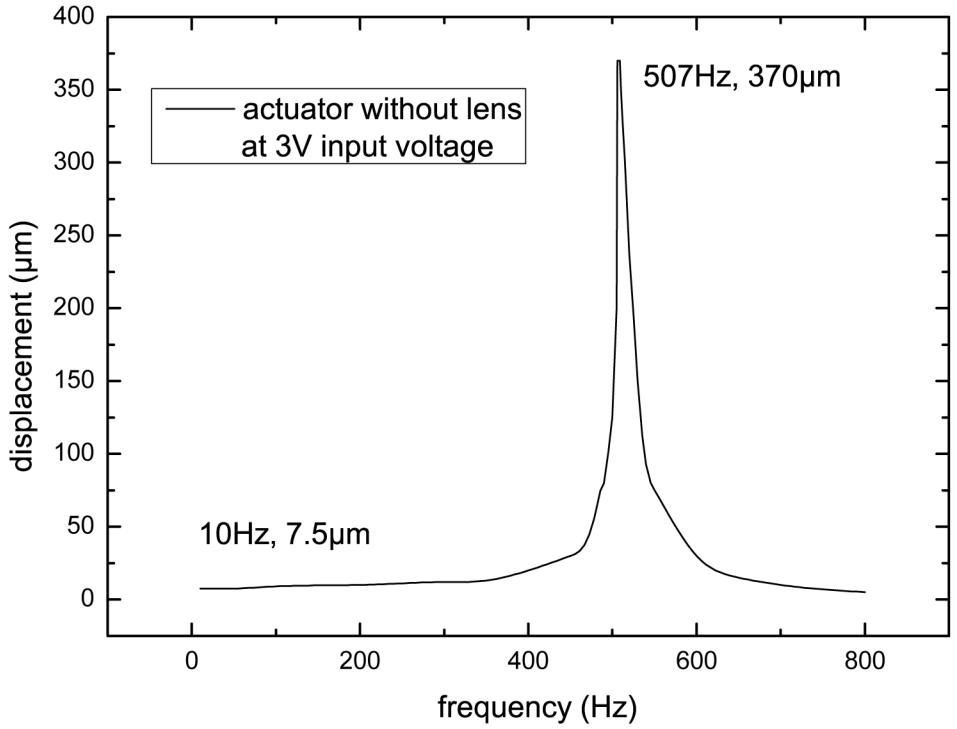

Figure 10.
Frequency sweep at 3 V input voltage, showing resonance peak at 507 Hz with displacement of 370 μm.

$watermark-text $watermark-text $watermark-text

Table 1

Comparison of existing in-planar translational miniature transmissions and actuators.

Source	Type	Max. Stroke (μm)	Cycle Freq. (Hz)	Cross-Sect. mm × mm.	Amplification
Faulhaber [6]	DC Linear	15000	300	6.8×6.8	N/A
Henderson [7]	Piezo wiggle	6000	5000	1.6×1.6	N/A
Smith et al. [8]	Modified comb	500	unreported	3×0.1	N/A
Hubbard et al. [9]	Thermal	52	230	2.5×1	3.5x
Conway et al. [10]	PZT	1.4	5000	0.5×0.54	10x
Kota et al. [11]	Comb drive	20	3880	<0.01×2	12x
Sabr et al. [12]	PZT stack	82	542	20×0.4	18x
Chu et al. [13]	Thermal	100	unreported	2×2	21x
Su and Yang [14]	Comb drive	10	unreported	0.7×0.7	148x
Current Paper	PZT Ceramic	486	507	3×0.6	170x

J Micromech Microeng. Author manuscript; available in PMC 2012 November 23.

$watermark-text

$watermark-text

$watermark-text

Table 2

Comparison of three platform suspension systems (k_t: transverse spring constant, k_v: vertical spring constant, k_l: lateral spring constant).

	Design 1	Design 2	Design 3
k_l	1.47 N/m	0.21 N/m	0.37 N/m
k_t	2.86 N/m	1.12 N/m	278 N/m
k_v	9.09 N/m	7.74 N/m	25 N/m
k_v/k_l	6.2	36	68
k_t/k_l	1.9	5.3	751
length	2.56 mm	2 mm	4 mm

$watermark-text

$watermark-text

$watermark-text

Table 3

Dimensions for optimized transmission and suspension.

lever springs width	12 μm
lever springs length	100 μm
dist. between lever springs	20 μm
short lever beam length	1200 μm
long lever beam length	4000 μm
chevron springs width	8 μm
chevron springs length	600 μm
chevron beam width	70 μm
chevron beam length	300 μm
chevron angle	60°
platform suspension width	8 μm
platform suspension length	2600 μm